Postprint of: Mazur Ł., Ignaczak J., Bik M., Molin S., Sitarz M., Gil A., Brylewski T., Effectiveness of a dual surface modification of metallic interconnects for application in energy conversion devices, INTERNATIONAL JOURNAL OF HYDROGEN ENERGY, Vol. 47, iss. 9 (2022), pp. 6295-6311, DOI: 10.1016/j.ijhydene.2021.11.256

Effectiveness of a dual surface modification of metallic interconnects for application in energy conversion devices

[1]Łukasz Mazur, [2]Justyna Ignaczak, [1]Maciej Bik, [2]Sebastian Molin, [1]Maciej Sitarz, [1]Aleksander Gil, [1]Tomasz Brylewski*

[1]AGH University of Science and Technology, Faculty of Materials Science and Ceramics, al. Mickiewicza 30, 30-059 Krakow, Poland

[2]Gdańsk University of Technology, Faculty of Electronics, Telecomunications and Informatics, ul. Narutowicza 11/12, 80-233 Gdańsk, Poland

Abstract

A dual surface modification of an SOFC metallic interconnect with a Gd_2O_3 layer and an $MnCo_2O_4$ coating was evaluated. The tested samples were oxidized for 7000 h in air at 1073 K. Oxidation products were characterized using XRD, SEM-EDS, and confocal Raman imaging, and ASR was measured. The effect of gadolinium segregation at grain boundaries in Cr_2O_3 was evaluated using S/TEM-EDS. Area specific-resistance was measured and fuel cell tests investigating electrochemical performance and Cr contamination of electrodes were also performed. The results show that the proposed dual modification was more advantageous than either modification applied separately. The fuel cell tests performed after aging in humidified hydrogen at 1073 K and involving an actual interconnect made of this dual-modified material showed that after 250 h of aging its electrochemical parameters were nearly identical to those

*Corresponding author at: AGH University of Science and Technology, Faculty of Materials Science and Ceramics, Al. Mickiewicza 30, 30-059 Krakow, Poland, Tel.: +48 12 6175229; fax.: +48 12 6172493. E-mail address: brylew@agh.edu.pl (T. Brylewski)

of the non-aged reference electrode. Moreover, the modification protected the electrodes from Cr poisoning.

Keywords: Solid oxide fuel cells (SOFC); Metallic interconnects; Oxidation kinetics; Microstructure; Electrical conductivity; Chromium poisoning

1. Introduction

The process of global warming resulting from the extensive use of fossil fuels may be slowed down by the use of more environmentally-friendly energy sources such as wind and solar power. However, the use of these forms of energy is highly dependent on weather conditions, which can cause fluctuations in the supplied electric energy [1]. Potential solutions to this problem include the use of systems based on solid oxide fuel cells (SOFCs) and electrolyzer cells (SOECs). SOFCs are capable of converting fuel, namely hydrogen, into electricity, while SOECs can be used for the reverse process [2]. These two types of devices can thus provide a balanced supply of electricity from renewable power sources, and allow power to be generated independently of the weather.

A major advantage of both SOFC and SOEC modes is that they utilize the same materials and design features with regard to the main components of a cell stack. These include the interconnect, porous oxygen and hydrogen electrodes, and a dense electrolyte [1,3,4]. The interconnect serves several functions – it provides mechanical support to the entire device, allows cells to be stacked, transports current and, last but not least, supplies gaseous reactants via its channels. Interconnects operate in very harsh conditions, namely high temperatures of above 873 K and under exposure to an oxidizing-reducing environment on the anode and cathode side. Consequently, in order for interconnects to last for ca. 40000 h – their expected lifetime – the materials that are used for their construction need to meet very

strict requirements. These include high chemical stability, i.e. lack of interactions with electrode materials, resistance to high-temperature corrosion in both oxidizing and reducing atmospheres, a thermal expansion coefficient that matches those of the remaining components of the cell, and a low area-specific resistance (ASR), which should not exceed 0.1 $\Omega \cdot cm^2$ [4-7]. Both metallic and ceramic materials can be used to manufacture SOFC interconnects. However, there is currently more interest in the use of metallic interconnects, especially ferritic stainless steels (FSS) with high chromium content, which are characterized by their low cost, ease of manufacturing, high thermal and electrical conductivity and, finally, match the remaining elements of the cell very well in terms of the thermal expansion coefficient [8-10].

Although the application of FSS has many advantages, it nevertheless poses certain challenges. As ferritic steel undergoes high-temperature corrosion, a protective Cr_2O_3 scale forms on its surface; its thickness gradually increases with SOFC operating time. The formation of this semiconducting phase leads to an increase in ASR. An excessively high electrical resistance caused by the growing scale can lead to a major decrease in stack efficiency [11-13]. Another issue associated with the application of ferritic steels is chromium evaporation. Chromium reacts with the gas components in the operating space of the electrodes. This leads to the formation of volatile chromium compounds, including CrO_3 and $CrO_2(OH)_2$ [14]. These compounds diffuse into the working space of the electrode and decompose on its surface, forming unwanted oxide phases. This process is known as electrode poisoning, since it results in the degradation of their electrochemical properties and the subsequent decrease in SOFC lifetime [15,16].

In order to improve the performance of interconnects based on ferritic steel, a number of modifications have been proposed so far. One way to limit the negative effects associated with the use of ferritic steels in high temperature conditions is surface modification. Such

modifications include the application of so-called "(re-)active elements" (e.g. Y, La, Ce, Gd). These metals reduce the growth rate of the Cr_2O_3 scale and also improve its adhesion to the metallic substrate [17,18]. A steel's surface can be modified in several ways. Active element ions can be implanted underneath the surface, or layers of nanoparticles of active element oxides can be deposited on the surface [19-21]. One of the possible explanations for the beneficial influence of active elements on the ferritic steels' resistance to high-temperature corrosion is that they cause the predominant oxidation mechanism to change from the outward diffusion of metal cations to the inward diffusion of oxidants [22-24]. This is associated with the segregation of active element molecules at grain boundaries, which entails that – in order to avoid an unnecessary increase in electrical resistance – the applied active element layer should be neither thick nor continuous [25]. Up to now, the active element most commonly studied from the perspective of application for the surface modification of metallic interconnects is yttrium [25-29]. Some authors, however, have reported that lanthanides such as Ce [29-32], Nd [19], La [19], and Gd [29,33] are significantly more effective that yttrium [19,29]. Gd_2O_3 has been shown to be particularly effective at reducing the oxidation rate of ferritic steels in conditions in which temperature fluctuates in cycles [29]. Lanthanide oxide layers were obtained by decomposing rare-earth metal phosphates deposited on the Crofer 22 APU ferritic steel via electrolysis or dip-coating [29]. Surface modification with other rare earth element oxides, including Y_2O_3, La_2O_3, or Nd_2O_3, have also been found to improve the corrosion resistance of the Crofer 22 APU ferritic steel when evaluated in studies involving over 100 h of oxidation in air at 1073 K [19]. The oxidation rates for samples after surface modification with the afore-mentioned three oxides are fairly similar, and are all slightly better than the oxidation rate measured for unmodified Crofer 22 APU (parabolic oxidation rate coefficients: Crofer 22 APU – 4.8×10^{-14} $g^2\cdot cm^{-4}\cdot s^{-1}$, Y_2O_3 – 1.1×10^{-14} $g^2\cdot cm^{-4}\cdot s^{-1}$, La_2O_3 – 0.9×10^{-14} $g^2\cdot cm^{-4}\cdot s^{-1}$, Nd_2O_3 – 1.0×10^{-14} $g^2\cdot cm^{-4}\cdot s^{-1}$). However, the electrical properties of

the steel/scale system for these samples differ to a much more noticeable extent. In the case of La_2O_3 and Nd_2O_3, the ASR was reduced to 0.004 and 0.016 $\Omega \cdot cm^2$, respectively, whereas an Y_2O_3 addition resulted in an increased ASR – 0.252 $\Omega \cdot cm^2$, as measured in air at 800°C [19].

Another way to improve the performance of SOFCs is by applying protective-conductive coatings onto the surface of the interconnect. Numerous chemical compounds have been investigated as potential materials for such oxide coatings, including the following: $La_{1-x}Sr_xCrO_3$ [34,35] and $La_{1-x}Ca_xCrO_3$ [34] perovskites, $Mn_xCo_{3-x}O_4$ [36-41], $Mn_{1+x}Cr_{2-x}O_4$ [41], and $Mn_{2-x}Co_{1+x}Me_x$ (where Me=Cu, Ni, or Fe) [42-45] spinels and M-Cr-Al-Y-O compounds (where M=Ti, Co and/or Mn) [46]. $Cu_xMn_{3-x}O_4$ systems have likewise been garnering increased interest [47-52]. Several methods of deposition, such as slurry spraying [53], screen printing [54,55], electroplating [56] or sputtering [57,58], were reported upon in recent studies. Taking into account the complicated shape of the bipolar plates arranged to form a system of channels that supply gas reactants to a particular working area of the SOFC stack, it seems that the use of the electrophoretic deposition method in combination with the appropriate thermal treatment should guarantee that uniform spinel coatings that do not exhibit any significant degree of open porosity are obtained [36,38,59-61]. Coatings based on manganese-cobalt spinel are especially popular owing to their unique transport properties. Studies indicate that the use of Mn-Co-O coatings with a spinel structure ensures that scale growth is reduced and strongly inhibits the rate of chromium evaporation. The fact that such layered systems have been shown to retain low area-specific resistance during long-term tests is another important advantage [62-65]. Work in this area of research has so far been geared towards the application of a single surface modification of ferritic steels, achieved using either active elements alone or via the deposition of spinel coatings containing an active element, including materials in the Mn-Co-Y-O system [55,66]. In each of these cases, improvements in both corrosion resistance and the electrical properties of the layered systems were

observed. However, the result achieved when the yttrium-containing spinel coating was applied was not spectacular, because the amount of yttrium incorporated into the crystal lattice of the manganese-cobalt spinel was insufficient to ensure the desired corrosion resistance of the newly obtained dual-layer interconnect material. The question therefore arises whether both ASR and the chromium evaporation rate can be kept at a sufficiently low level via a single modification via the deposition of active elements or protective-conductive coatings, considering the long operating time of SOFCs. This is especially true of the cathode side of the SOFC, which is exposed to very aggressive reaction conditions.

The first attempt to combine the deposition of nanoparticles of active element oxides with the electrophoretic deposition of spinel coating proved to be a success [33]. During the first step of the performed procedure, the surface of unoxidized Crofer 22 APU was dip-coated to deposit a layer of gadolinium nitrate, which transformed into layer consisting of Gd_2O_3 nanoparticles during the applied thermal treatment. The steel modified in this way was coated with a$MnCo_2O_4$ layer via electrophoresis. The layered system obtained as described was characterized by a lower oxidation rate, lower ASR, and reduced chromium evaporation rate in comparison to all previously studied layered systems [33]. However, these promising results were obtained for a relatively short oxidation time of 1000 h [33]. To comprehensively verify these results in a proper long-term oxidation study, further research was required.

Consequently, the present study investigated the effect of a double modification of the interconnect surface, which involved the deposition of a thin layer of Gd_2O_3 and the electrophoretic deposition of $MnCo_2O_4$ coating, on the electrical properties, oxidation products as well as the electrode poisoning caused by chromium. For this purpose, samples were oxidized for 7000 h in an air atmosphere at 1073 K – the operating temperature of SOFCs. The oxidation products were investigated using both conventional methods and certain state-of-the-art techniques like atomic-resolution scanning transmission electron

microscopy as well as confocal Raman imaging, which is rarely used in this type of research and yet shows great potential. In order to determine the effect of electrode poisoning by chromium, a novel approach to the exposure of the electrode to the evaporating Cr was undertaken. Until now, the interconnect had been placed directly on top of the electrode when conducting cell aging tests [67]. However, this does not reflect the actual position of the interconnect in a cell. In the modified method, the sample representing the interconnect was placed at a certain distance from the electrode surface [68]. This allows the ability of the applied coatings to mitigate chromium evaporation to be determined with far more precision. Finally, the performance of the fuel cell based on the developed material was also tested.

2. Experimental section

2.1. Preparation of ferritic steel

The material used as the steel substrate was the Crofer 22 APU ferritic steel (Thyssen Krupp VDM GmbH, Germany). The chemical composition of the investigated steel, expressed in wt%, is presented in Table 1.

The samples had a rectangular shape, with dimensions of 20×10×1mm. Prior to use, the metallic substrates were polished using SiC abrasive paper graded from 1000 to 2000-grit.

Table 1. Chemical composition of the Crofer 22 APU steel (wt%) [69].

Steel	Chemical composition [wt%]										
	Cr	Fe	C	S	Mn	Si	Al	Ti	La	P	Cu
min.	20.0	Bal.			0.30			0.03	0.04		
max.	24.0		0.03	0.02	0.80	0.50	0.50	0.20	0.20	0.05	0.50

The samples were washed in acetone in an ultrasonic bath. Before deposition, each sample was pre-treated for 1 hour in air at 1073 K. This pre-oxidation stage was applied to

reduce the growth rate of the intermediate reaction layer between the steel substrate and the coating, formed as a result of the outward diffusion of Fe and Cr [70].

2.2. Deposition of Gd_2O_3 layer

Dip-coating was applied to deposit gadolinium oxide on the ferritic steel surface. The procedure utilized a gadolinium nitrate solution with a concentration of 0.1 M, prepared from an analytical grade $Gd(NO_3)_3 \times 6H_2O$ reagent supplied by Sigma Aldrich and ethyl alcohol supplied by POCH Poland S.A. – likewise of analytical grade. The metallic substrates underwent three immersions, each lasting 10 s. After the first two immersions, the substrates were heated for 15 min in air at 673 K in order to decompose the gadolinium nitrate and obtain gadolinium oxide. After the last immersion, the samples were heated for 30 minutes under the same conditions.

2.3. Electrodeposition of $MnCo_2O_4$ coating and thermal treatment procedures

Two types of Crofer 22 APU substrates were coated with manganese-cobalt spinel via electrophoretic deposition. One substrate was unmodified steel, while the other one was a steel sample which had gadolinium oxide nanoparticles deposited on it by means of dip-coating. The solution applied during electrophoresis was prepared specifically for the procedure using a commercially available $MnCo_2O_4$ spinel powder (**fuelcell** materials). A 50:50 mixture of ethanol (Chempur, 99.8%) and isopropanol (Chempur, min. 99.7%) was used to synthesize a powder suspension with a 1 wt% concentration. Iodine (0.5 $g \cdot dm^{-3}$, Sigma-Aldrich, ≥99.8%) acted as the dispersant. Zirconia balls were also added to the suspension, which then underwent 5 days of homogenization, and was also additionally homogenized for 15 minutes in an ultrasonic bath just before the electrophoretic deposition, increasing homogeneity even further. The conditions of the electrophoretic deposition were as

follows: voltage – 60 V, distance between the electrodes – 10 mm, deposition time – 30s. The applied electrophoretic process yielded fully homogeneous and reproducible coatings, which were subsequently dried for 10 h in air at 353 K. The samples were then heated over two separate stages – first for 2 h in an Ar+10% H_2 mixture at 1173 K, and then for 4 h in air 900°C. This ensured that the spinel coatings had the desired density.

2.4. Long-term oxidation tests

Tests were conducted for four different types of samples: unmodified steel, steel that had a thin layer of gadolinium oxide, steel with a manganese-cobalt spinel coating, and a steel sample that had received both of the afore-mentioned modifications. These samples are subsequently referred to as Crofer 22 APU, Crofer 22 APU/Gd, Crofer 22 APU/MC, and Crofer 22 APU/Gd/MC, respectively.

Oxidation was performed in laboratory air at a temperature of 1073 K and under cyclic temperature conditions, in a horizontal tube furnace. The total oxidation time was 7000 h. The oxidation kinetics of the samples were measured using thermogravimetry – by determining the mass gain after time intervals ranging from 160 to 290 h. To allow this, they were first removed from the furnace and left to cool to ambient temperature, after which they were weighed with a Radwag XA 210 laboratory balance (accuracy – 1.0×10^{-5} g).

2.5. Phase composition and morphology studies

The X'Pert Pro diffractometer with CuKα radiation was used to determine the phase composition of the tested samples.

The morphology and chemical composition of the surfaces and cross-sections of the samples were analyzed by means of scanning electron microscopy (SEM) with energy dispersive X-ray analysis (EDS). A Phenom XL (Thermo Fisher Scientific) desktop SEM

equipped with an integrated energy dispersive X-ray (EDX) microanalyzer was used for this purpose. Imaging was performed at an accelerating voltage of 10 kV using backscattered electron detection, whereas the EDX analyses were performed using a 15 kV electron beam. For cross-sectional analysis, the samples were vacuum-mounted in an epoxy resin (Struers EpoFix) and polished down to a 1 μm finish (Struers Tegramin-20 system with Struers consumables).

2.6. Confocal Raman imaging

In order to dispel any uncertainties concerning the phase composition of the investigated multilayered system, Raman spectroscopy was also applied. The WITec alpha 300 M+ spectrometer (air-cooled solid-state 488 nm laser, ZEISS Epiplan-Neufluar objective (100×/0.9 NA), UHTS 300 spectrograph, 600 grooves·mm^{-1} grating, and Andor CCD detector) and the WITec Control FIVE software were used to perform confocal Raman imaging of the Crofer 22 APU/Gd/MC sample – a 20×20 μm region was investigated using 2s of acquisition time per spectrum and 0.5 μm sampling density. This region was in the close vicinity of the site on the cross-section where SEM images had been taken and EDS mapping had been done. In total, 1600 Raman spectra were acquired within the 120-1800cm^{-1} range and with a 3.0 cm^{-1} spectral resolution. Subsequently, the data was pre-processed with the WITec Project FIVE 5.3 PLUS software according to the standard protocol, including baseline correction (3rd polynomial order) and cosmic spike removal (CRR filter). Two types of analyses were then carried out to obtain the chemical concentration maps. Firstly, the *k*-means cluster analysis (KMC) was performed to receive so-called cluster maps and corresponding average spectra of the defined classes. Secondly, an integration filter (with the given position and width of the band) was used for characteristic spectral regions (i.e. the 1597 cm^{-1} band for carbon present in the conductive resin); this made it possible to generate

the chemical distribution maps and the corresponding average spectra. Both methods yielded the same results.

2.7. Transmission electron microscopic observation

The ZEISS NEON CrossBeam 40EsB was used to prepare a lamella for microscopic observations via the focused ion beam (FIB) technique. Since the dimensions of the lamella cannot exceed 10×7 μm, the first step was to remove the protective-conducting spinel layer from an area in the reaction zone in the material using the gallium beam. The lamella was then cut from the sample and thinned in a Fischione NanoMill 1060 to a thickness of 40 nm, which was thin enough to allow an electron beam to pass through.

S/TEM investigations were conducted by means of an atomic-resolution Titan Cubed G2 60-300 S/TEM microscope with the ChemiSTEM system (FEI), operated by the AGH UST International Centre of Electron Microscopy for Materials Science. The microscope is equipped with a state-of-the-art X-FEG electron source based on field emission and a dodeca-pole corrector of the spherical aberration of magnetic condenser lenses, which gives it a resolution of up to 70 pm at an accelerating voltage of 300 kV [71]. When operating the device in the S/TEM mode, a high-angle annular dark-field (HAADF) detector was used. Energy-dispersive X-ray spectroscopy (S/TEM-EDS) was applied for the analysis of the material's chemical composition.

2.8. Area-specific resistance measurements

Area-specific resistance – defined as the product of resistance and the contact surface area of the oxide and the steel – is commonly used as a measure of the electrical resistance of a material which had undergone oxidation. The symmetrical design of the samples allowed

the area-specific resistance of the samples to be calculated from the obtained values of resistance by means of the formula:

$$ASR = \frac{R \cdot A}{2} \quad (1)$$

where: R – electrical resistance [Ω] and A – surface area of the Pt contact layer [cm^2].

In order to measure the electrical resistance of the oxidation products, a DC 2-probe 4-point method was used. The measurements took place while the samples were cooling from 1073 to 623 K. Additional details regarding the entire procedure may be found in another paper [68].

2.9. Aging and fuel cell tests

To determine the influence of the interconnect coating on the electrochemical performance of the fuel cellsas well as its ability to block chromium evaporation, an interconnect with the dual-modified surface (Crofer 22 APU/Gd/MC) and an uncoated interconnect (Crofer 22 APU) were placed in a tube furnace together with anode-supported solid oxide fuel cells (ASC-SOFCs, Taipei Tech, Taipei, Taiwan) and aged for 250 h at 1073 K. Humidified air (3 vol% H_2O) flowed (100 $ml \cdot min^{-1}$) through the furnace continuously. Each applied cell had a diameter of 2.54 cm and consisted of a Ni-YSZ porous support, a Ni-YSZ active electrode, a 25-μm-thick YSZ electrolyte, an 8-μm-thick CGO diffusion barrier layer, and a 30-μm-thick LSCF ($La_{0.6}Sr_{0.4}Co_{0.2}Fe_{0.8}O_{3-d}$) oxygen electrode with an active surface area of 1 cm^2. The electrochemical performance of the aged cells with interconnects was then characterized and compared with that of two types of reference cells – a "fresh" cell, as-received from the producer – and a cell aged for 250 h to mimic the same conditions to which the aged cells with interconnects had been applied. The procedure applied for this purpose assesses the potential gas-transport-induced chemical poisoning of the oxygen

electrode of the cells (LSCF) and can be used as an indicator of the vaporization of Cr species relevant to solid oxide fuel cell operation. It is described in more detail in previous studies [67,68].

Fuel cell tests were performed in an OpenFlange V5 setup from Fiaxel Sarl, Lausanne, Switzerland. The setup featured dedicated Cr-free contacting elements, which is why the presence of Cr in the electrodes could only be attributed to aging. The fuel cell tests were performed using dry H_2 from a hydrogen generator (LNI, Switzerland) and dry, compressed air, with a 100 $ml \cdot min^{-1}$ flow in both cases. For electrochemical characterization, the Solartron 1260 frequency response analyzer coupled with the Solartron 1287 potentiostat/galvanostat (Solartron Analytical, Leicester, UK) were used. Impedance spectroscopy was measured at open circuit voltage (OCV), using an excitation voltage of 10 mV and over a range of frequencies from 100 kHz to 0.1 Hz. Data analysis was performed using the ZView 3.2 application (Scribner Associates, USA).

3. Results and discussion

3.1. Oxidation kinetics

Figure 1 presents the oxidation kinetics for the Crofer 22 APU sample (unmodified steel) as well as the modified samples (Crofer 22 APU/Gd, Crofer 22 APU/MC, Crofer 22 APU/Gd/MC), recorded over 7000 h of oxidation in air at 1073 K. The results are shown both in a linear (Fig. 1A) and parabolic (Fig. 1B) presentation, and represent mass gain per unit area in a function of oxidation time.

The plots indicate that the oxidation of all examined samples approximately follows the parabolic rate law, which entails that the diffusion of reagents in the scale is the slowest process that determines the oxidation rate [72,73]. The ferritic steel sample that had undergone a dual surface modification (Crofer 22 APU/Gd/MC) clearly exhibited the highest

resistance to oxidation, whereas – as expected – the opposite can be said of unmodified steel (Crofer 22 APU).

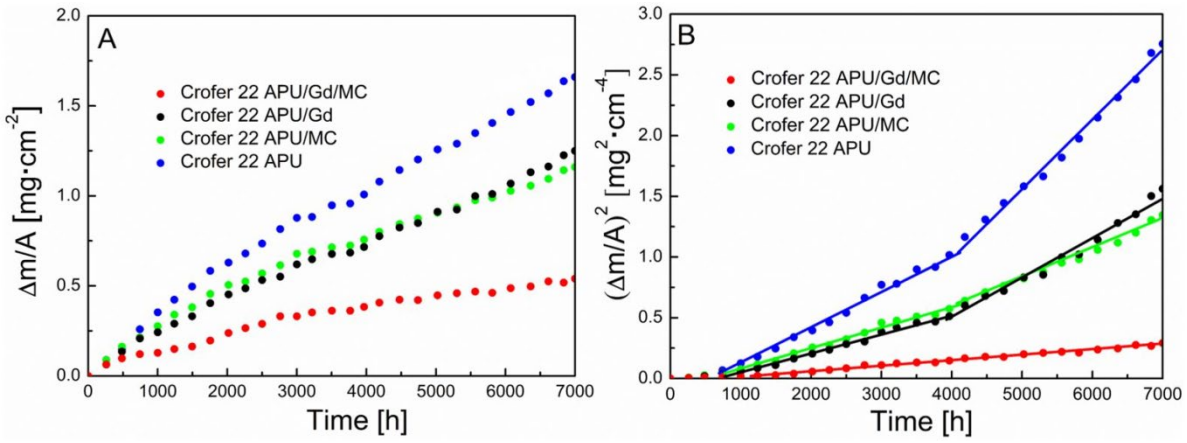

Figure. 1. Oxidation kinetics plots for investigated samples oxidized over 7000 h in air at 1073 K: A) linear plot, B) parabolic plot.

In the case of the samples with single modifications (Crofer 22 APU/Gd and Crofer 22 APU/MC), the oxidation rates were similar. It is worth mentioning that although the Gd_2O_3 nanoparticles deposited on the steel were slightly more effective than the MC spinel layer at protecting the material against oxidation over the first 5050 h, this trend reversed in the remaining 1950 h, with the sample modified with the MC layer eventually having a somewhat lower mass gain at the end of the test period.

These data are reflected by the parabolic rate constants (k_p) estimated for the samples by means of the Pilling-Bedworth equation (2) [72]:

$$\left(\frac{\Delta m}{A}\right)^2 = k_p \cdot t + C \qquad (2)$$

where: $\Delta m/A$ – mass gain per unit area [$g \cdot cm^{-2}$], k_p – parabolic rate constant [$g^2 \cdot cm^{-4} \cdot s^{-1}$], t – reaction time [s], and C – integration constant, a measure of deviation from parabolic oxidation kinetics in the initial stage.

The parabolic rate constants, the time intervals in which the samples obeyed the parabolic rate law, and the correlation coefficients (r) from regression analyses are listed in Table 2.

Table 2. Parabolic oxidation rate constants of the samples oxidized for 7000 h in air at 1073 K.

Sample	**Time interval of compliance with parabolic rate law [h]**	**k_p [$g^2 \cdot cm^{-4} \cdot s^{-1}$]**	**r**
Crofer 22 APU	480-4000 4000-7000	8.22×10^{-14} 1.53×10^{-13}	0.9961 0.9943
Crofer 22 APU/MC	490-3800 3800-7000	4.65×10^{-14} 6.57×10^{-14}	0.9942 0.9964
Crofer 22 APU/Gd	490-4000 4000-7000	4.18×10^{-14} 9.01×10^{-14}	0.9937 0.9907
Crofer 22 APU/Gd/MC	0-1750 1750-7000	5.58×10^{-15} 1.21×10^{-14}	0.9835 0.9935

It should be noted that two stages with different oxidation rates were observed for every sample (Fig. 1B). Interestingly enough, in the case of the dual-modified steel the oxidation rate in the second stage is significantly lower than for all other samples (Table 2). It had been concluded in a previous paper [33] that Gd_2O_3 nanoparticles deposited on steel can reduce the oxidation rate – however, the long-term oxidation study showed that for longer periods of over 4000 h it is highly recommended that the MC spinel layer also be applied, since the latter can provide an effective barrier against high-temperature oxidation, and acts in synergy with the former modification (Fig. 1, Table 2). Indeed, the oxidation rate constant of the Crofer 22 APU that had undergone a dual surface modification is lower by as much as an entire order of magnitude than the constant determined for the unmodified steel. Moreover, the parabolic oxidation rate constant determined for this dual-modified steel was lower than the k_p values reported in studies dealing with the oxidation kinetics of ferritic steels classified as chromia

formers, which have been the materials of choice in the production of SOFC interconnects. For reference, the k_p value reported for the Crofer 22 APU with a deposited $MnCo_2O_4$ after merely 1000 h of oxidation at 1073 K in ref. [74] is 3.90×10^{-14} $g^2\cdot cm^{-4}\cdot s^{-1}$, whereas the value given in ref. [39] is 0.64×10^{-14} $g^2\cdot cm^{-4}\cdot s^{-1}$. In the case of the $Mn_{1.5}Co_{1.5}O_4$ coating deposited on the same steel and oxidized over the same time interval, the reported k_p values include 1.45×10^{-14} $g^2\cdot cm^{-4}\cdot s^{-1}$ [75] – for the oxidation temperature of 1073 K – and 7.30×10^{-13} $g^2\cdot cm^{-4}\cdot s^{-1}$ [55] – when the oxidation temperature was 923 K. These values are much higher than those determined for the samples studied in the present work and oxidation times ranging from 0 to 1750 h (Table 2). One of the papers on the subject investigated longer oxidation times of up to 4500 h and the k_p value its authors determined for Crofer 22 APU samples with an $MnCo_2O_4$ coating was slightly lower than the value observed in the present paper. However, it should be emphasized that the difference in oxidation times was rather significant – 2500 h.

3.2. Morphology and phase composition

After the oxidation of the four studied samples, scanning electron microscopic observations combined with XRD investigations were conducted to determine what oxidation products had formed as well as the thickness and composition of the corresponding layers. The SEM images of sample cross-sections and the obtained XRD patterns are shown in Figure 2.

Upon examination of the specimens' surface, different morphological structures were found. For unmodified steel, two types of grains were observed – smaller oval grains and larger grains with well-formed growth planes. Some grain agglomerates were also present. The image of the cross-section (Fig. 2A) showed that the scale was composed of two layers.

The bottom layer consisted of Cr_2O_3, while the top one was formed by a mixture of Mn_2O_3 and $(Mn,Cr)_3O_4$.

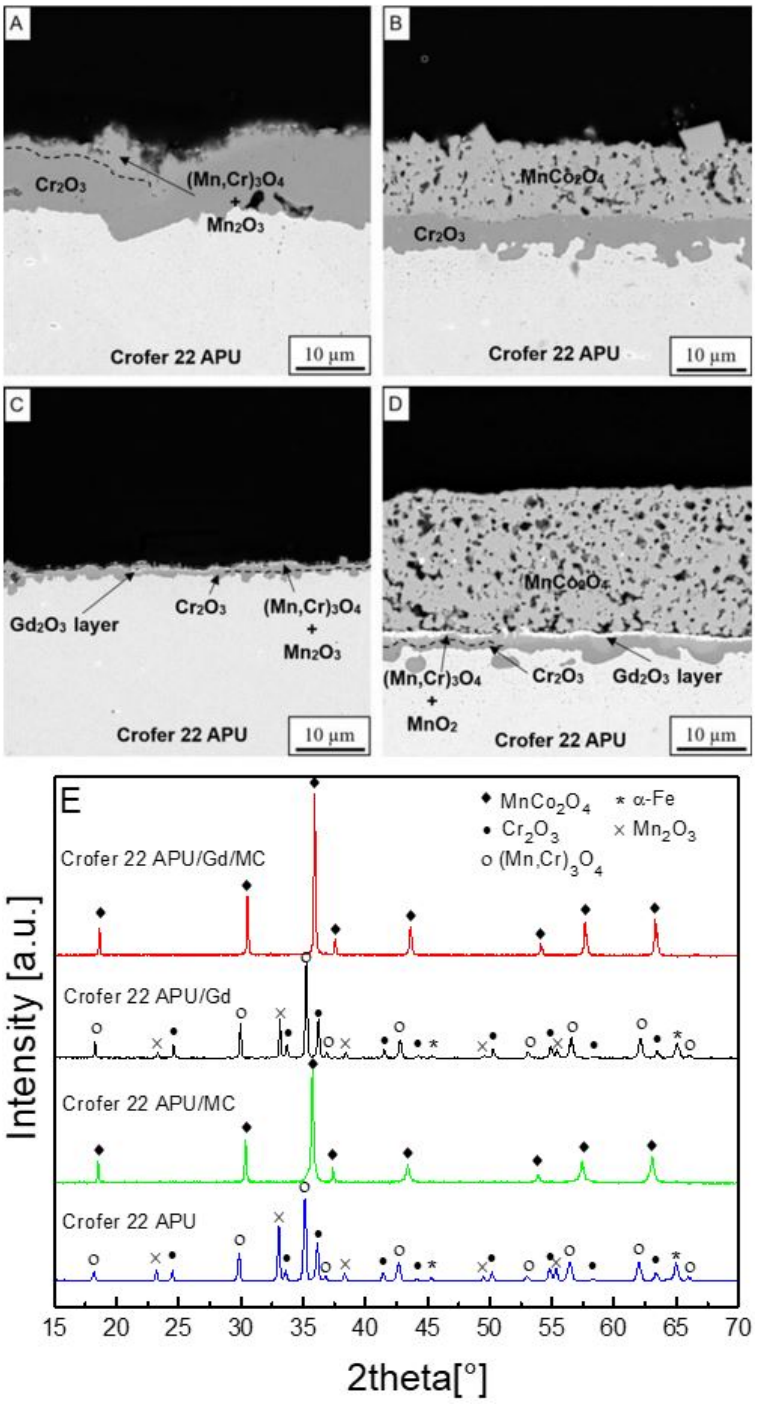

Figure 2. SEM micrographs of polished sample cross-sections and the X-ray diffraction patterns recorded for the studied samples after 7000 h of oxidation in air at 1073 K:

A) Crofer 22 APU, B) Crofer 22 APU/MC, C) Crofer 22 APU/Gd,

D) Crofer 22 APU/Gd/MC, E) X-ray diffraction patterns.

These phases were identified by means of XRD (Fig. 2E). The presence of manganese-chromium spinel had been reported earlier [76] and is associated with its high thermodynamic stability at 1073 K. Manganese oxide formed due to the manganese content of the steel, since it is used as an alloying additive. The thickness of the formed scale varied between 9 and 12.5 μm, which was bound to significantly affect the ASR value.

Observations of the surface of the Crofer 22 APU/MC sample revealed uniformly distributed, fine grains of the coating material and a small number of well-formed $(Mn,Co)_3O_4$ crystals. The only phase detected via XRD diffraction studies (Fig. 2E) was the $MnCo_2O_4$ spinel with a cubic structure, i.e. the coating material. The sole presence of the spinel phase suggests that the coating was continuous and did not contain secondary phases that might have been the result of interactions with chromium. This is important in the context of reducing chromium evaporation rates. Indeed, a high coating density and low number of closed pores was indicated by the cross-section shown in the Fig. 2B. However, SEM-EDS also revealed the presence of a Cr_2O_3 intermediate reaction layer with a thickness that varied from 3.5 to 4.5 μm and good adhesion to the metallic core.

The third type of sample, i.e. Crofer 22 APU/Gd, exhibited similarity to unmodified steel in terms of phase composition (Fig. 2E). The SEM micrograph of the cross-section this sample (Fig. 2C) likewise revealed two layers; however, the thickness of the scale was far lower than in the case of unmodified steel – between1.1 and 2.3 μm at the site where the Gd_2O_3 layer was found (represented by the thin white layer), and around 8.5 μm over areas without the Gd_2O_3 layer underneath. The perovskite phase of $GdCrO_3$, which had been found in the authors' previous study that featured a shorter oxidation time, was not observed [33]. A possible explanation is that the perovskite phase might have been "obscured" by other oxidation products formed over the considerably longer oxidation time applied in the present study. It should also be emphasized that the deposited layer of Gd_2O_3 nanoparticles was not

continuous, as confirmed by observations of the surface. Although the amount of this compound was sufficient for it to effectively perform its function, it was nevertheless too small to produce a signal from the afore-mentioned secondary perovskite phase strong enough to be detected using XRD. This phase was only eventually confirmed using the applied confocal Raman spectroscopy technique (see section 2.4).

As for the sample obtained via dual modification (Crofer 22 APU/Gd/MC), the XRD study showed the sole presence of cubic $MnCo_2O_4$ (Fig. 2E). As in the case of steel with the spinel coating, this was an indication that the spinel phase had not reacted with the chromium in the intermediate reaction layer, and secondary phases that could be attributed to such reactions were not present. Observations of the surface revealed uniformly distributed, fine grains of spinel. The cross-section micrograph (Fig. 2D), in turn, showed that the obtained coating was dense, significantly reducing the chromium evaporation rate. In the presented cross-section, a well-formed Gd_2O_3 layer could be distinguished. Below this layer, the presence of a two-layer scale was also shown to be present by SEM-EDS. The bottom layer consisted of Cr_2O_3, while the top one was formed by a mixture of MnO_2 and $(Mn,Cr)_3O_4$ (Section 2.4). The scale formed between the protective coating and the metallic core had a thickness of between 1.5-3.5 μm (a thicker scale had formed due to the presence of cavities in the steel) and had good adhesion to the metallic core.

Morphological observations combined with phase composition studies provided valuable information about the oxidation products formed in the case of each sample, especially with regard to electrical properties. However, it can occasionally be very hard to determine the phase composition of the oxidation products and correlate this information with the morphological observations. To fully investigate oxidation products in more complex systems, complementary techniques are required (see sections 3.3 and 3.4).

3.3. Transmission electron microscopic observations

Atomic-resolution S/TEM observations were carried out for a region of the reaction zone in the steel sample after dual modification (Crofer 22 APU/Gd/MC) – at the site where the layer composed of Cr_2O_3 had been found. Figure 3A shows the triple junction between grains in chromia, whereas Figures 3B and 3C show the respective areas marked with squares under increasing magnification.

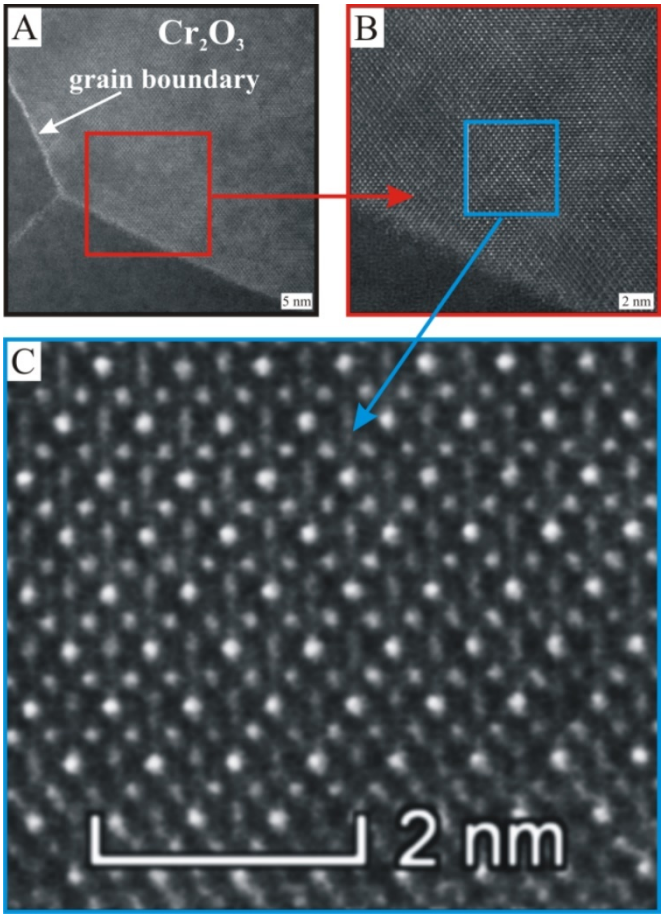

Figure 3. Triple junction in Cr_2O_3 grains – S/TEM-HAADF image (A) and respective areas marked with squares under increasing magnification (B, C).

Element distribution maps of gadolinium (Fig. 4B) and chromium (Fig. 4C) were then obtained using S/TEM-EDS in the grain boundary area. EDS line scan analysis was also performed for Gd, Cr and O (Fig. 4D) along a line perpendicular to the grain boundary (white dotted line in Fig. 4A).

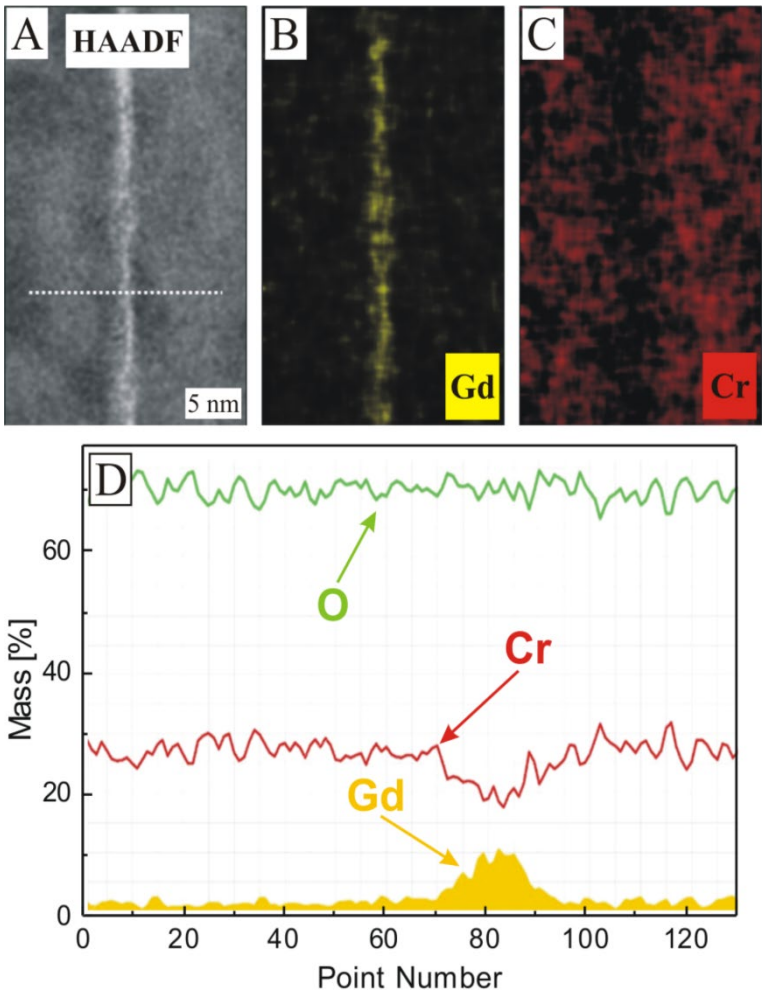

Figure 4. S/TEM-HAADF image of the grain boundary (A), element distribution maps of Gd and Cr determined via S/TEM-EDS(B,C), and EDS line scan analysis for Gd, Cr and O across the white dotted line in Fig. 5A (D).

The performed investigations showed that the grain boundaries in chromia have higher gadolinium content than grain interiors. This finding is significant, since the segregation of active elements at grain boundaries in Cr_2O_3 had been found to improve the oxidation resistance of alloys that form protective chromia scales via what is known as the reactive element effect (REE) [77,78].

This effect was first observed in the 1920s for Ni-Cr alloys with a small alloying addition consisting of a mixture of active elements [79]. Subsequent research found that this effect also occurs when the ions of an active element are implanted into the surface layer of

alloys that form protective Cr_2O_3 scales, when it is applied in the form of nanoparticles in a material's bulk in the case of oxide dispersion-strengthened (ODS) alloys [80,81], or when it is applied in the form of layer of nanoparticles on an alloy's surface [19,25,29].

The present study shows that the segregation of active elements at grain boundaries in chromia is still observed after oxidation times as long as 7000 h. It should be noted that Gd_2O_3 segregation reduces the oxidation rate by a significant factor (see section 3.1), yet at the same time the presence of this compound in the form of precipitates prevents the ASR of the investigated layered system from being overly affected (see section 3.5). This phenomena can be very significant from the standpoint of application in SOFC interconnects.

3.4. Confocal Raman imaging

Figure 5 illustrates the results of applying confocal Raman imaging to study the cross-section of the oxidized steel sample after dual modification (Crofer 22 APU/Gd/MC). This particular area was chosen for Raman imaging (Fig. 5A) due to the fact that SEM observations and EDS analyses were performed in its close vicinity and confirmed the occurrence of discernible layers of Mn-Co spinel and Gd-based phases (Fig. 2). The application of two alternative techniques (KMC – Fig. 5B and integration filter – Fig. 6C) unambiguously confirmed the presence of five different phases in the studied specimen (Fig. 5D), aside from the graphite-like carbon originating from the mounting resin (Fig. 5E; bands at 1379 and 1597 cm^{-1} [82]), which filled the pores of the protective spinel coating.

Starting with the top layer in the multilayered system, the presence of the protective coating based on $MnCo_2O_4$ (marked in blue) is confirmed based on the occurrence of bands at ca. 155, 480, 520, and 600 cm^{-1} (the most intense) [83-86]. Even though bands within 670-690 cm^{-1} are usually considered the most characteristic for different types of spinel-type oxides [87], in the above-cited works the presence of similar spinel structures was proved

without these bands being observed, using a similar temperature of spinel formation. Their disappearance may be mostly due to the fact that most Mn cations occupy octahedral sites within the spinel structure, which results in both the broadening and a shift of bands towards a lower Raman shift than is generally observed [83,84]. Therefore, in this case the $MnCo_2O_4$ protective spinel may be assumed to be present. Underneath the spinel phase, the next, nearly continuous layer (marked in red) can be discerned. Five distinctive bands at ca. 208, 490, 620 (the most intense and characteristic) and 668 cm^{-1} may be attributed to the perovskite-type oxide phase with possible $GdCr_{1-x}Mn_xO_3$ stoichiometry, where x is very likely equal to ca. 0.7-0.8.

Such high content of Mn^{3+} cations was deduced not only from spectra recorded in [88-90], but also from the broadness and high intensity of both bands at 620 and 668 cm^{-1}, which suggest the occurrence of the so-called Jahn-Teller effect, frequently induced by the presence of Mn^{3+} cations within the perovskite structure [87]. Taking into account the authors' previous work [33] (in which the formation of similar perovskite ($GdCrO_3$) was observed), the presence of Gd_2O_3 confirmed therein was also expected. However, in this case, the absence of a pronounced characteristic band at around 360 cm^{-1} [91] strongly suggests that this phase was likewise not present. Nevertheless, it should be noted that even if the imaging was conducted in a representative area of this specimen, Raman measurements are local in character, hence it is impossible to state beyond any doubt that gadolinium oxide was absent.

Underneath the protective coatings, two other layers were distinguished. In the case of the first one (marked in green), bands attributed to the $(Mn,Cr)_3O_4$ spinel phase [87] were observed at around 196, 515 and 681 cm^{-1} (the most intense and characteristic), while bands attributed to MnO_2 (ramsdellite/nsutite) [92,93] were observed at 538, 579 along with 635 cm^{-1} (the most characteristic).

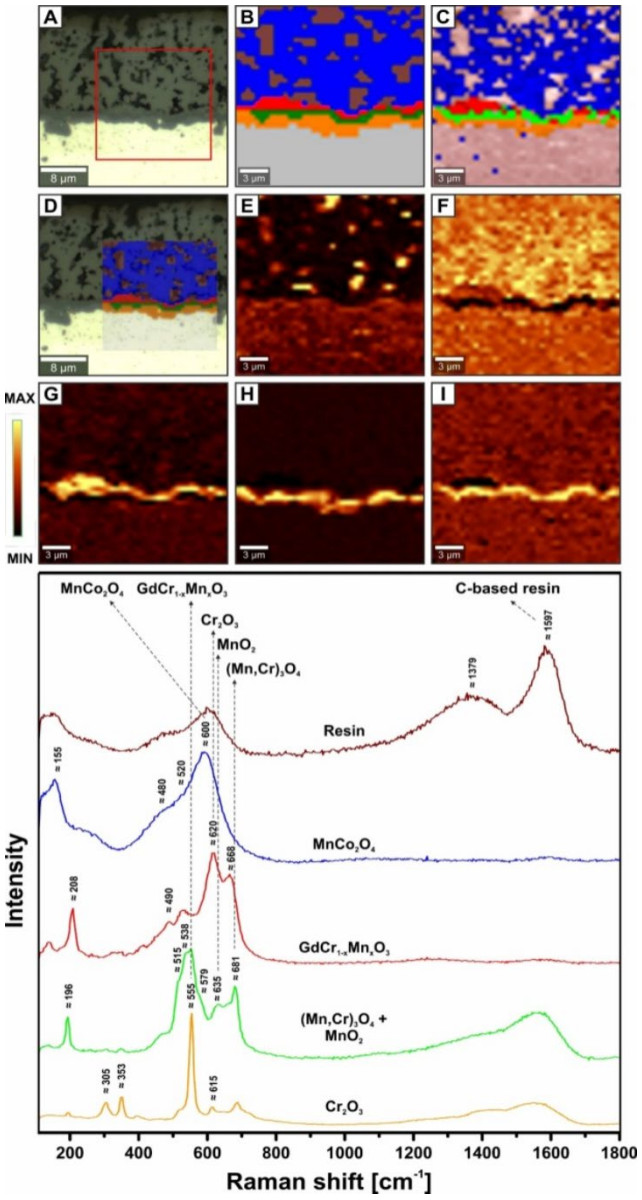

Figure 5. Confocal Raman imaging of the cross-section of the Crofer 22 APU/Gd/MC sample oxidized at 1073 K for 7000h: A) confocal image (red square corresponds to area investigated with Raman laser), B) *k*-means cluster analysis, C) combined distribution image, D) overlay bitmap for images A and B. Raman distribution images (obtained via the integration of the most characteristic band for a particular phase along with the value of its Raman shift given in brackets) are complemented with the average Raman spectra: E) resin (1597 cm^{-1}), F) $MnCo_2O_4$ (600 cm^{-1}), G) $GdCr_{1-x}Mn_xO_3$ (620 cm^{-1}), H) Cr_2O_3 (555 cm^{-1}), I) $(Mn,Cr)_3O_4$ (681 cm^{-1}) / MnO_2 (538 cm^{-1}). Each average spectrum is also marked with bands that can be unequivocally attributed to the corresponding phase(s).

Neither the KMC nor the filter integration technique was able to differentiate the distribution of these two phases, as both bands responsible for Mn-O vibrations cannot be completely separated from the spectrum. This suggests that an MnO_2 minority phase can be homogenously distributed within the Mn-Cr spinel layer, which is known to nucleate during the oxidation of the Crofer 22APU steel [94]. In the case of the second layer (marked in orange), slightly thicker than the mixed Mn-Cr spinel+MnO_2 one, bands were observed at ca. 305, 353, 555 (the most intense and characteristic) and 615 cm^{-1}, and these can be considered to definitely originate from Cr_2O_3 [95]. In summary, the extremely wide spectrum of possibilities offered by a method like confocal Raman imaging is evident. Despite being non-destructive and both time- and cost-efficient, its popularity in investigations of the phase composition of samples oxidized at high temperatures remains low.

3.5. Area-specific resistance

Figure 6 shows the temperature dependence of area-specific resistance (ASR), as measured in air at temperatures in the range of 623-1073 K for the investigated samples oxidized for 7000 h in air at 1073 K.

The linear increase in ASR with temperature suggests that in the case of the studied samples charge transport is thermally activated. Assuming that small polaron hopping takes place in these samples, their area-specific resistance may be expressed as follows [6]:

$$ASR = \frac{A}{T} \cdot \exp\left(\frac{-E_c}{kT}\right) \tag{3}$$

where: A – pre-exponential factor [$\Omega \cdot cm^{-2} \cdot K^{-1}$], E_c – activation energy [$kJ \cdot mol^{-1}$], k – Boltzmann constant [$eV \cdot K^{-1}$], and T – absolute temperature.

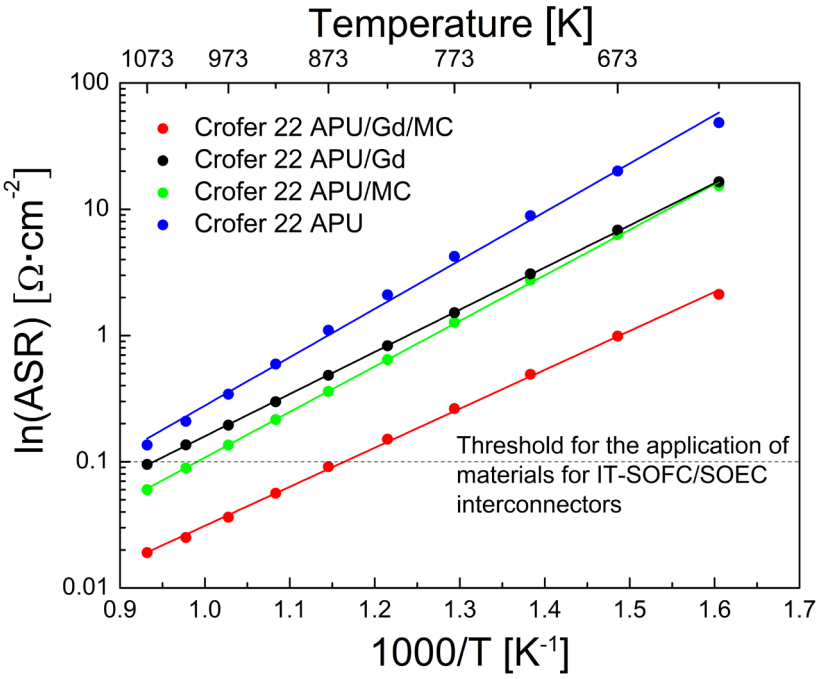

Figure 6. Temperature dependence of area-specific resistance for tested layered systems after 7000 h of oxidation in air at 1073 K, presented in an Arrhenius plots.

These data show that the steel sample that had undergone dual surface modification Crofer 22 APU/Gd/MC) was characterized by the lowest ASR across all measurement temperatures, while the opposite was true of unmodified steel. These differences grew less pronounced as measurement temperature increased. Intermediate ASR values were measured for the two samples that underwent single surface modifications – Crofer 22 APU/MC and Crofer 22 APU/Gd – with the latter exhibiting slightly higher area-specific resistance. The differences between the values observed for these two samples grew broader as measurement temperature increased.

Table 3 lists the ASR values measured for the investigated samples as well as their activation energies of electrical conduction, as determined from the ln(ASR/T) = f(1/T) linear dependences in the temperature range of 623-1073 K.

Table 3. Area-specific resistance (ASR) at 1073 Kand activation energy of electrical conduction (E_a) for the investigated layered systems after 7000 h of oxidation in air at 1073 K.

Material	ASR at 1073 K [Ω·cm^2]	E_a [eV]
Crofer 22 APU	0.1356	0.63
Crofer 22 APU/MC	0.0600	0.60
Crofer 22 APU/Gd	0.0951	0.56
Crofer 22 APU/Gd/MC	0.0190	0.50

As expected, the lowest ASR values over the entire investigated range were observed for the dual-modified sample (Crofer 22 APU/Gd/MC). For the samples that underwent single modifications, these values were still below the ASR threshold for interconnect materials, i.e. 0.1 Ω·cm^2 [96]. However, they were much higher than that obtained for the dual-modified sample. This may be related to the fact that the dual modification significantly reduced the growth rate of the Cr_2O_3 scale and, consequently, its thickness. On the other hand, the scale formed on the unmodified steel was the thickest. Cr_2O_3 itself has low electrical conductivity of (~0.01 S·cm^{-1}) and even the formation of an Mn-Cr-O spinel layer (~0.05 S·cm^{-1}) does not improve conductivity to any significant degree [76]. The ASR of the tested systems can therefore be concluded to strongly depend on scale thickness, since all scales formed on them had satisfactory adhesion to the ferritic steel substrate upon completion of the 7000-hour oxidation test. This was evident both from the determined oxidation kinetics and the observed morphology of the samples (see sections 2.1, 2.2 and 2.4). A clear correlation between the ASR values and the activation energy of electrical conduction can be observed when analyzing the data obtained for all investigated samples – both parameters are the lowest for the steel sample after dual modification and the highest for the unmodified steel (Table 3).

When the obtained ASR values are compared with the literature data, it is clear that the proposed dual modification improves this parameter. For example, the ASR reported for the

Crofer 22 H surface-modified with an $Mn_{1.5}Co_{1.5}O_4$ spinel coating after 1200 h of oxidation at 1073 was 0.0527 $\Omega \cdot cm^2$ [97]. The ASR of a layered system consisting of this coating deposited on a Crofer 22 APU substrate after 1000 h of oxidation at 1073 K was 0.013 $\Omega \cdot cm^2$ [39]. For longer oxidation times and depending on the method used to deposit this coating on the substrate, several different ASR values were obtained: 0.020 $\Omega \cdot cm^2$ – for 2500 h [36], 0.014 $\Omega \cdot cm^2$ – for 4000 h [63], and 0.020-0.050 $\Omega \cdot cm^2$ – for 5000 h [37]. After 1000 h of oxidation at 1023 K, a layered system with an $MnCo_2O_4$ spinel coating deposited on the Crofer 22 APU exhibited an ASR of ca. 0.005 $\Omega \cdot cm^2$ [58], whereas for the same temperature and an even longer oxidation time of 5000 h its ASR was 0.017 $\Omega \cdot cm^2$ [64]. The ASR obtained after the dual modification proposed in the present work is either below the above-cited values or just slightly above them – in the latter case, however, this is mostly due to the shorter oxidation times investigated in the cited works.

The obtained results show that applying the proposed dual modification helped increase the margin between the threshold set for materials applied in SOFC interconnects and the actual ASR value measured, even after 7000 h of oxidation in 1073 K. Maintaining a low ASR value over extended periods is a step towards reaching the target SOFC operating time of 40000 h, and may help reduce production costs and promote wider commercialization.

3.6. Aging and fuel cell test results

Since the target application of the investigated steel/coating layered system is the construction of SOFC stacks, it was necessary to take into consideration the effect of the proposed modification on the electrochemical properties of the LSCF cathode material operating in the electrochemical cell mode.

Figure 7 presents the current voltage (I-V) and power density (PD) curves (Fig. 7A) as well as Nyquist plots obtained via impedance spectroscopy (EIS) (Fig. 7B) for the cells

operating at 1073 K, with continuously flowing synthetic air as the oxidant and dry hydrogen as fuel.

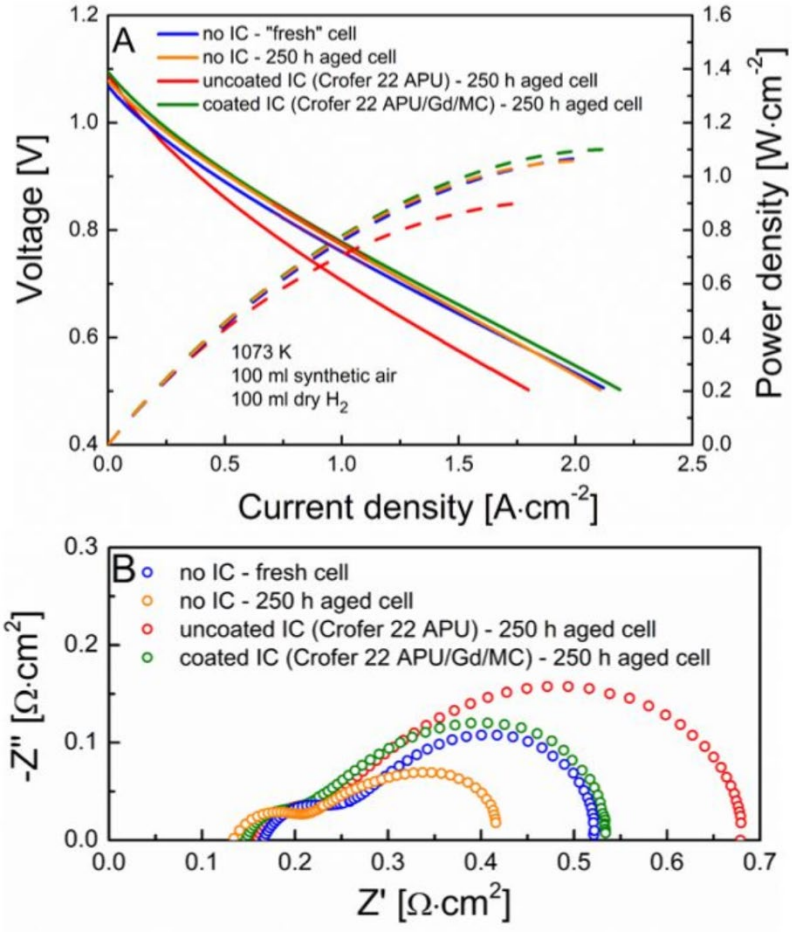

Figure 7. Plots recorded for the examined cells at 1073 K: A) I-V curves, B) Nyquist plot (IC – interconnect).

There were no pronounced differences in the current-voltage characteristics (Fig. 7A) between the "fresh" cell, the aged cell with no interconnect and the aged cell with the dual-modified interconnect (Crofer 22 APU/Gd/MC). All cells exhibited an open circuit voltage (OCV) of ~1.075 V and a maximum power density (P_{max}) of ~1.1 W·cm^{-2} at 1073 K. Aging the cell with the uncoated interconnect (Crofer 22 APU) for 250 h leads to a ~20% decrease in maximum power density – to ~0.9 W·cm^{-2} – which makes the necessity of applying a protective coating evident.

The comparison of the presented values with the literature data revealed certain differences with regard to the power density of the cells. For example, in paper [67] the maximum power density observed for a cell aged by placing it in the proximity of an interconnect with an Mn-Co-O spinel coating for 100 h and setting the temperature to 1073 K was 0.95-0.98 $W \cdot cm^{-2}$. The cell investigated in the cited paper was composed of the LSM material instead of the LSCF applied in the present study. However, paper [68] reported a study featuring an LCSF cathode aged for 250 h at a slightly lower temperature, i.e. 1023 K, placed near a steel interconnect consisting of the Crofer 22 APU substrate with an $Mn_{1.5}Co_{1.5}O_4$ coating. The power density of this cell was reported to be ca. 0.71-0.72 $W \cdot cm^{-2}$.

Electrochemical impedance spectroscopy (EIS) (Fig. 7B) performed at OCV revealed that the cells exhibited comparable ohmic resistance (R_{ohm}) in the range of 0.14-0.16 $\Omega \cdot cm^2$. However, while the fresh cell and the aged cell with the dual-modified interconnect were both characterized by a polarization resistance [67,68] (R_{pol}) of ~0.4 $\Omega \cdot cm^2$, this parameter increased significantly for the aged cell with the uncoated interconnect – to ~0.54 $\Omega \cdot cm^2$. The polarization resistance of the aged cell without the interconnect is visibly lower (~0.28 $\Omega \cdot cm^2$), but this is believed to have been caused by higher humidity of the hydrogen gas due to saturated drying stage of the hydrogen generator (confirmed afterwards by drying the columns). This can be confirmed further by calculating the tangent ASR values of the cells based on the I-V plots (Fig. 7A). The ASR can be calculated via a linear fit in the current density range of 0.7 $A \cdot cm^{-2}$ and 1.1 $A \cdot cm^{-2}$, in which the I-V curves are linear. For these measurement conditions, the humidity of the fuel gas will play a small role, as steam is generated during the current flow. Even though the power density will be lower due to the slight shift in OCV, the tangent ASR values can be used to compare cell performance in a reliable manner (given relatively small differences in fuel gas humidity). The ASR values for the "fresh" cell, the aged cell with no interconnect and the aged cell with the dual-modified

interconnect were 0.248 Ω·cm^2, 0.256 Ω·cm^2 and 0.252 Ω·cm^2, respectively. The ASR for the aged cell with uncoated interconnect was higher – 0.287 Ω·cm^2. The tangent ASR value confirms the protective properties of the coated interconnects in fuel cell tests.

3.7. Post-mortem microstructural characterization

After the electrochemical tests, polished cross-sections of the cells were analyzed by means of SEM-EDX to determine whether any Cr poisoning of the oxygen electrode had occurred. Figure 8 shows the SEM images of fuel cell cross-sections after 250h of aging at 1073 K, taken for the cell with the dual-modified interconnect (Crofer 22 APU/Gd/MC) (Fig. 8A), the cell with the uncoated interconnect (Crofer 22APU) (Fig. 8B), and the cell without interconnect (Fig. 8C), as well as the results of EDX point analyses for these three cells.

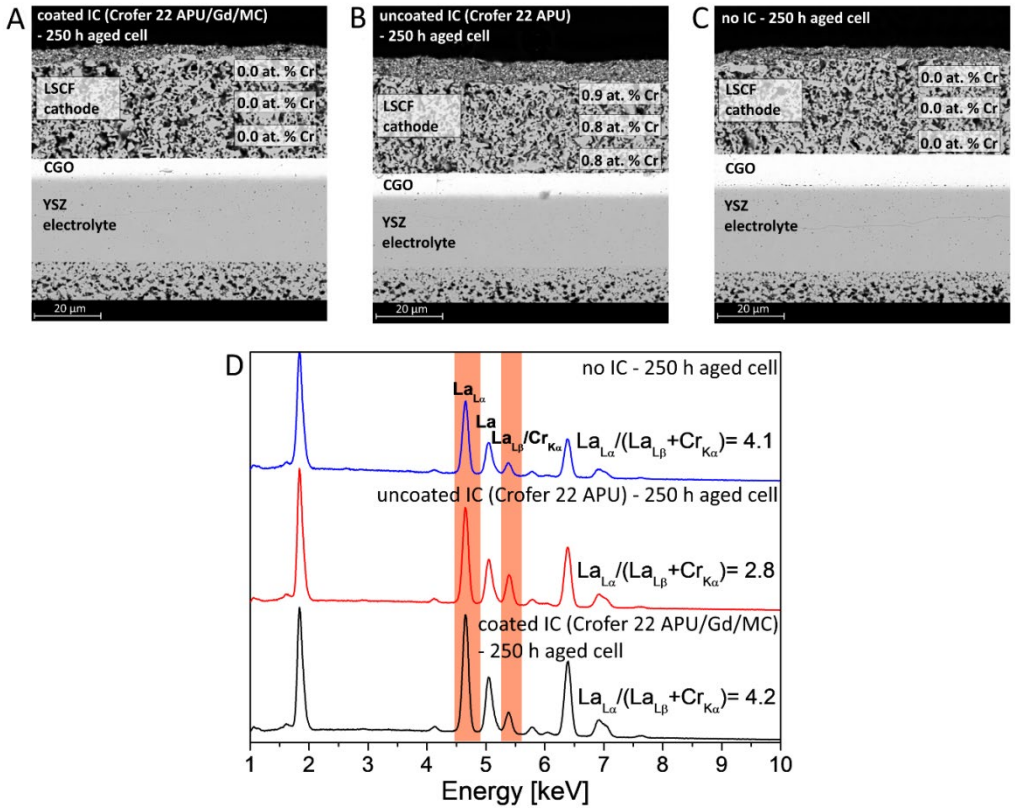

Figure 8. Post-mortem SEM images taken for: A) aged fuel cell with Crofer 22 APU/Gd/MC interconnect, B) aged fuel cell with Crofer 22 APU interconnect,
C) aged fuel cell without an interconnect, D) EDX spectra for the studied samples.

EDX analysis performed for LSCF cathode layer, which directly faced the uncoated steel interconnect, indicated the presence of chromium (Fig. 8B). Chromium content across this cathode layer was uniform and around ~0.8-0.9 at %. For comparison, EDX analysis did not reveal the presence of chromium in the cathode layer facing the dual-modified interconnect (Fig. 8A), nor did it find any chromium for the electrode in the aged cell with no interconnect, which served as the reference (Fig. 8C).

Due to the overlapping peaks of $Cr_{K\alpha}$ and $La_{L\beta}$ (Fig. 8D), it is difficult to establish the chromium content in the LSCF perovskite via EDX. However, the relative intensity ratio of $La_{L\alpha}/(La_{L\beta}+Cr_{K\alpha})$ can be used to confirm that chromium content has changed [98]. For the cathode layer of the aged reference cell, this ratio was 4.1 and in the case of the aged cell with the dual-modified interconnect it was 4.2, whereas for the one with uncoated interconnect the corresponding value was 2.8. This confirmed that the cathode layer of the latter cell was the only one that contained chromium.

4. Conclusions

The study aimed to evaluate if a dual-surface modification of materials for SOFC metallic interconnects – in this case one that involved the deposition of nanoparticles of Gd_2O_3 – a reactive element – and a cubic $MnCo_2O_4$ spinel protective coating can bring with it any advantages over a single modification via only one of the two afore-mentioned methods used to improve oxidation resistance. Dip-coating was used to deposit the gadolinium oxide nanoparticles, while the spinel coatings were deposited electrophoretically. The performed long-term tests involving 7000 h of oxidation in air at 1073 K showed that, when applied concurrently, the two modifications allowed the thickness of the corrosion product and thereby the parabolic rate constant of oxidation to be reduced significantly in comparison to both unmodified steel and steel samples with single modifications, and yielded the highest

resistance to corrosion. The dual-modified steel also proved to exhibit the lowest area-specific resistance value – far below the threshold for materials designed for application in SOFC interconnects. The observations conducted using the Titan Cubed G2 60-300 S/TEM microscope for this sample revealed that gadolinium oxide nanoparticles deposited on the surface of a high-chromium ferritic steel consistently improve oxidation resistance owing to the segregation of gadolinium at grain boundaries in the Cr_2O_3 scale formed between the steel and the spinel layer. An associated effect is the significantly improved adhesion of the chromia scale to the metallic phase. Confocal Raman imaging provided unambiguous information about the phase composition – based on the integration of characteristic bands, the existence of a multilayered system consisting of $MnCo_2O_4$/$GdCr_{1-x}MnO$/ $(Mn,Cr)_3O_4$+MnO_2/Cr_2O_3 scale was confirmed, and the method also allowed each phase to be located within the cross-sectional microstructure with high-precision. Based on the electrochemical and post-mortem microstructural characterization of fuel cells aged for 250 h in humidified hydrogen at 1073 K and a non-aged reference cell, it was established that the aged cell with the dual-modified interconnect was similar to the non-aged reference one in terms of performance. No Cr could be found in the LSCF oxygen electrode layer of the former cell, proving that no poisoning of the electrode had occurred and that the dual modification provided effective protection against the evaporation of Cr species.

Conflicts of interest

There are no conflicts to declare.

Acknowledgements

Financial support from the National Science Centre, project No. 2015/19/B/ST8/01094, is gratefully acknowledged. This work was partly supported with a subsidy from the Ministry of

Education and Science for AGH University of Science and Technology in Kraków (Project No. 16.16.160.557).

Highlights

- Crofer 22 APU underwent single and dual modifications via dip-coating and/or EPD
- Dual modification reduced the oxidation rate to a larger degree than single ones
- Confocal Raman imaging allowed the phase compositions to be identified
- ASR of dual-modified material after 7000 h of oxidation was excellent
- Dual modification effectively protected electrode materials from Cr poisoning

5. Bibliography

[1] Ni M, Leung MKH, Leung DYC. Technological development of hydrogen production by solid oxide electrolyzer cell (SOEC). Int J Hydrogen Energy 2008;33:2337-54. https://doi.org/10.1016/j.ijhydene.2008.02.048.

[2] Chaubey N, Wani BN, Bharadwaj SR, Chattopadhyaya MC. Physicochemical properties of rare earth doped ceria $Ce_{0.9}Ln_{0.1}O_{1.95}$ (Ln = Nd, Sm, Gd) as an electrolyte material for IT-SOFC/SOEC. Solid State Sci 2013;20:135-41. https://doi.org/10.1016/j.solidstatesciences.2013.03.020.

[3] Laguna-Bercero MA. Recent advances in high temperature electrolysis using solid oxide fuel cells: A review. J Power Sources 2012;203:4-16. https://doi.org/10.1016/j.jpowsour.2011.12.019.

[4] Molenda J, Kupecki J, Baron R, Blesznowski M, Brus G, Brylewski T, et al. Status report on high temperature fuel cells in Poland – Recent advances and achievements. Int J Hydrogen Energy 2017;42:4366-403. https://doi.org/10.1016/j.ijhydene.2016.12.087.

[5] Quadakkers WJ, Piron-Abellan J, Shemet V, Singheiser L. Metallic interconnectors for solid oxide fuel cells- A review. Mater High Temp 2003;20:115-27. https://doi.org/10.3184/096034003782749071.

[6] Yang Z, Weil KS, Paxton DM, Stevenson JW. Selection and Evaluation of Heat-Resistant Alloys for SOFC Interconnect Applications. J Electrochem Soc 2003;150:A1188. https://doi.org/10.1149/1.1595659.

[7] Hu YZ, Yao SW, Li CX, Li CJ, Zhang SL. Influence of pre-reduction on microstructure homogeneity and electrical properties of APS $Mn_{1.5}Co_{1.5}O_4$ coatings for SOFC interconnects. Int J Hydrogen Energy 2017;42:27241-53. https://doi.org/10.1016/j.ijhydene.2017.09.073.

[8] Linderoth S, Hendriksen P V., Mogensen M, Langvad N. Investigations of metallic alloys for use as interconnects in solid oxide fuel cell stacks. J Mater Sci 1996;31:5077-82. https://doi.org/10.1007/BF00355908.

[9] Hassan MA, Mamat O Bin, Mehdi M. Review: Influence of alloy addition and spinel coatings on Cr-based metallic interconnects of solid oxide fuel cells. Int J Hydrogen Energy 2020;45:25191-209. https://doi.org/10.1016/j.ijhydene.2020.06.234.

[10] Puranen J, Pihlatie M, Lagerbom J, Salminen T, Laakso J, Hyvärinen L, et al. Influence of powder composition and manufacturing method on electrical and chromium barrier properties of atmospheric plasma sprayed spinel coatings prepared from $MnCo_2O_4$ and Mn_2CoO_4 + Co powders on Crofer 22 APU interconnectors. Int J Hydrogen Energy 2014;39:17246-57. https://doi.org/10.1016/j.ijhydene.2014.08.016.

[11] Zhu WZ, Deevi SC. Opportunity of metallic interconnects for solid oxide fuel cells: A status on contact resistance. Mater Res Bull 2003;38:957-72. https://doi.org/10.1016/S0025-5408(03)00076-X.

[12] Fergus JW. Metallic interconnects for solid oxide fuel cells. Mater Sci Eng A

2005;397:271-83. https://doi.org/10.1016/j.msea.2005.02.047.

[13] Brylewski T, Nanko M, Maruyama T, Przybylski K. Application of Fe-16Cr ferritic alloy to interconnector for a solid oxide fuel cell. Solid State Ionics 2001;143:131-50. https://doi.org/10.1016/S0167-2738(01)00863-3.

[14] Tan KH, Rahman HA, Taib H. Coating layer and influence of transition metal for ferritic stainless steel interconnector solid oxide fuel cell: A review. Int J Hydrogen Energy 2019;44:30591-605. https://doi.org/10.1016/j.ijhydene.2019.06.155.

[15] Hilpert K, Das D, Miller M, Peck DH, Weiß R. Chromium Vapor Species over Solid Oxide Fuel Cell Interconnect Materials and Their Potential for Degradation Processes. J Electrochem Soc 1996;143:3642-7. https://doi.org/10.1149/1.1837264.

[16] Matsuzaki Y, Yasuda I. Dependence of SOFC Cathode Degradation by Chromium-Containing Alloy on Compositions of Electrodes and Electrolytes. J Electrochem Soc 2001;148:A126. https://doi.org/10.1149/1.1339869.

[17] Pfeil LB. Improvement of heat-resisting alloys. Patent no 459848, 1937.

[18] Pillis MF, Correa OV, de Araújo EG, Ramanathan LV. Oxidation behavior of FeCr and FeCrY alloys coated with an aluminium based paint. Mater Res 2008;11:251-6. https://doi.org/10.1590/S1516-14392008000300004.

[19] Fontana S, Amendola R, Chevalier S, Piccardo P, Caboche G, Viviani M, et al. Metallic interconnects for SOFC: Characterisation of corrosion resistance and conductivity evaluation at operating temperature of differently coated alloys. J Power Sources 2007;171:652-62. https://doi.org/10.1016/j.jpowsour.2007.06.255.

[20] Qu W, Li J, Ivey DG. Sol-gel coatings to reduce oxide growth in interconnects used for solid oxide fuel cells. J Power Sources 2004;138:162-73. https://doi.org/10.1016/j.jpowsour.2004.06.063.

[21] Cabouro G, Caboche G, Chevalier S, Piccardo P. Opportunity of metallic interconnects

for ITSOFC: Reactivity and electrical property. J Power Sources 2006;156:39-44. https://doi.org/10.1016/j.jpowsour.2005.08.039.

[22] Whittle DP, Stringer J. Improvements in high temperature oxidation resistance by additions of reactive elements or oxide dispersions. Philos Trans R Soc London Ser A, Math Phys Sci 1980;295:309-29. https://doi.org/10.1098/rsta.1980.0124.

[23] Moon DP. Role of reactive elements in alloy protection. Mater Sci Technol (United Kingdom) 1989;5:754-64. https://doi.org/10.1179/mst.1989.5.8.754.

[24] Stringer J. The reactive element effect in high-temperature corrosion. Mater Sci Eng A 1989;120-121:129-37. https://doi.org/10.1016/0921-5093(89)90730-2.

[25] Molin S, Persson H, Skafte TL, Smitshuysen AL, Jensen SH, Andersen KB, et al. Effective yttrium based coating for steel interconnects of solid oxide cells: Corrosion evaluation in steam-hydrogen atmosphere. J Power Sources 2019;440. https://doi.org/10.1016/j.jpowsour.2019.226814.

[26] Gil A, Kryshtal O, Brylewski T, Czyrska-Filemonowicz A. Characterization of a Cr_2O_3 scale formed on chromium with implanted yttrium ions by advanced electron microscopy. Surf Coatings Technol 2019;368:232-42. https://doi.org/10.1016/j.surfcoat.2019.03.081.

[27] Cueff R, Buscail H, Caudron E, Riffard F, Issartel C, El Messki S. Effect of reactive element oxide coating on the high temperature oxidation behaviour of FeCrAl alloys. Appl Surf Sci 2004;229:233-41. https://doi.org/10.1016/j.apsusc.2004.01.072.

[28] Riffard F, Buscail H, Caudron E, Cueff R, Issartel C, Perrier S. Yttrium sol-gel coating effects on the cyclic oxidation behaviour of 304 stainless steel. Corros Sci 2003;45:2867-80. https://doi.org/10.1016/S0010-938X(03)00114-8.

[29] Gil A, Wyrwa J, Brylewski T. Improving the Oxidation Resistance and Electrical Properties of Ferritic Stainless Steels for Application in SOFC Interconnects. Oxid Met

2016;85:151-69. https://doi.org/10.1007/s11085-015-9605-9.

[30] Alman DE, Jablonski PD. Effect of minor elements and a Ce surface treatment on the oxidation behavior of an Fe-22Cr-0.5Mn (Crofer 22 APU) ferritic stainless steel. Int J Hydrogen Energy 2007;32:3743-53. https://doi.org/10.1016/j.ijhydene.2006.08.032.

[31] You PF, Zhang X, Zhang HL, Liu HJ, Zeng CL. Effect of CeO2 on oxidation and electrical behaviors of ferritic stainless steel interconnects with Ni–Fe coatings. Int J Hydrogen Energy 2018;43:7492-500. https://doi.org/10.1016/j.ijhydene.2018.02.178.

[32] Mosavi A, Ebrahimifar H. Investigation of oxidation and electrical behavior of AISI 430 steel coated with Mn–Co–CeO_2 composite. Int J Hydrogen Energy 2020;45:3145-62. https://doi.org/10.1016/j.ijhydene.2019.11.183.

[33] Brylewski T, Molin S, Marczyński M, Mazur, Domaradzki K, Kryshtal O, et al. Influence of Gd deposition on the oxidation behavior and electrical properties of a layered system consisting of Crofer 22 APU and $MnCo_2O_4$ spinel. Int J Hydrogen Energy 2021;46:6775-91. https://doi.org/10.1016/j.ijhydene.2020.11.169.

[34] Fergus JW. Lanthanum chromite-based materials for solid oxide fuel cell interconnects. Solid State Ionics 2004;171:1-15. https://doi.org/10.1016/j.ssi.2004.04.010.

[35] Brylewski T, Dabek J, Przybylski K, Morgiel J, Rekas M. Screen-printed (La,Sr)CrO 3 coatings on ferritic stainless steel interconnects for solid oxide fuel cells using nanopowders prepared by means of ultrasonic spray pyrolysis. J Power Sources 2012;208:86-95. https://doi.org/10.1016/j.jpowsour.2012.02.015.

[36] Smeacetto F, De Miranda A, Cabanas Polo S, Molin S, Boccaccini D, Salvo M, et al. Electrophoretic deposition of $Mn_{1.5}Co_{1.5}O_4$ on metallic interconnect and interaction with glass-ceramic sealant for solid oxide fuel cells application. J Power Sources 2015;280:379-86. https://doi.org/10.1016/j.jpowsour.2015.01.120.

[37] Molin S, Sabato AG, Bindi M, Leone P, Cempura G, Salvo M, et al. Microstructural

and electrical characterization of Mn-Co spinel protective coatings for solid oxide cell interconnects. J Eur Ceram Soc 2017;37:4781-91. https://doi.org/10.1016/j.jeurceramsoc.2017.07.011.

[38] Bobruk M, Molin S, Chen M, Brylewski T, Hendriksen P V. Sintering of $MnCo_2O_4$ coatings prepared by electrophoretic deposition. Mater Lett 2018;213:394-8. https://doi.org/10.1016/j.matlet.2017.12.046.

[39] Molin S, Sabato AG, Javed H, Cempura G, Boccaccini AR, Smeacetto F. Co-deposition of CuO and $Mn_{1.5}Co_{1.5}O_4$ powders on Crofer22APU by electrophoretic method: Structural, compositional modifications and corrosion properties. Mater Lett 2018;218:329-33. https://doi.org/10.1016/j.matlet.2018.02.037.

[40] Talic B, Venkatachalam V, Hendriksen PV, Kiebach R. Comparison of $MnCo_2O_4$ coated Crofer 22 H, 441, 430 as interconnects for intermediate-temperature solid oxide fuel cell stacks. J Alloys Compd 2020;821. https://doi.org/10.1016/j.jallcom.2019.153229.

[41] Chen X, Hou PY, Jacobson CP, Visco SJ, De Jonghe LC. Protective coating on stainless steel interconnect for SOFCs: Oxidation kinetics and electrical properties. Solid State Ionics 2005;176:425-33. https://doi.org/10.1016/j.ssi.2004.10.004.

[42] Brylewski T, Kruk A, Bobruk M, Adamczyk A, Partyka J, Rutkowski P. Structure and electrical properties of Cu-doped Mn-Co-O spinel prepared via soft chemistry and its application in intermediate-temperature solid oxide fuel cell interconnects. J Power Sources 2016;333:145-55. https://doi.org/10.1016/j.jpowsour.2016.09.136.

[43] Zanchi E, Talic B, Sabato AG, Molin S, Boccaccini AR, Smeacetto F. Electrophoretic co-deposition of Fe_2O_3 and $Mn_{1,5}Co_{1,5}O_4$: Processing and oxidation performance of Fe-doped Mn-Co coatings for solid oxide cell interconnects. J Eur Ceram Soc 2019;39:3768-77. https://doi.org/10.1016/j.jeurceramsoc.2019.05.024.

[44] Xiao J, Zhang W, Xiong C, Chi B, Pu J, Jian L. Oxidation behavior of Cu-doped $MnCo_2O_4$ spinel coating on ferritic stainless steels for solid oxide fuel cell interconnects. Int J Hydrogen Energy 2016;41:9611-8. https://doi.org/10.1016/j.ijhydene.2016.03.051.

[45] Park BK, Lee JW, Lee SB, Lim TH, Park SJ, Park CO, et al. Cu- and Ni-doped $Mn_{1.5}Co_{1.5}O_4$ spinel coatings on metallic interconnects for solid oxide fuel cells. Int J Hydrogen Energy 2013;38:12043-50. https://doi.org/10.1016/j.ijhydene.2013.07.025.

[46] Gannon P, Deibert M, White P, Smith R, Chen H, Priyantha W, et al. Advanced PVD protective coatings for SOFC interconnects. Int J Hydrogen Energy 2008;33:3991-4000. https://doi.org/10.1016/j.ijhydene.2007.12.009.

[47] Shao Y, Ding JT, Guo PY, Ou WX, Mao SY, Huang MR, et al. High temperature characteristics and phase compositions of Cu/Mn multilayers with the different average thickness prepared by electrodeposition. J Alloys Compd 2021;871. https://doi.org/10.1016/j.jallcom.2021.159439.

[48] Sun Z, Wang R, Nikiforov AY, Gopalan S, Pal UB, Basu SN. $CuMn_{1.8}O_4$ protective coatings on metallic interconnects for prevention of Cr-poisoning in solid oxide fuel cells. J Power Sources 2018;378:125-33. https://doi.org/10.1016/j.jpowsour.2017.12.031.

[49] Ignaczak J, Naumovich Y, Górnicka K, Jamroz J, Wróbel W, Karczewski J, et al. Preparation and characterisation of iron substituted $Mn_{1.7}Cu_{1.3-x}Fe_xO_4$ spinel oxides (x = 0, 0.1, 0.3, 0.5). J Eur Ceram Soc 2020;40:5920-9. https://doi.org/10.1016/j.jeurceramsoc.2020.07.001.

[50] Wei P, Deng X, Bateni MR, Petric A. Oxidation and electrical conductivity behavior of spinel coatings for metallic interconnects of solid oxide fuel cells. Corrosion 2007;63:529-36. https://doi.org/10.5006/1.3278404.

[51] Hosseini N, Abbasi MH, Karimzadeh F, Choi GM. Development of $Cu_{1.3}Mn_{1.7}O_4$ spinel coating on ferritic stainless steel for solid oxide fuel cell interconnects. J Power Sources 2015;273:1073-83. https://doi.org/10.1016/j.jpowsour.2014.10.017.

[52] Joshi S, Petric A. Nickel substituted $CuMn_2O_4$ spinel coatings for solid oxide fuel cell interconnects. Int J Hydrogen Energy 2017;42:5584-9. https://doi.org/10.1016/j.ijhydene.2016.08.075.

[53] Yang Z, Xia GG, Li XH, Stevenson JW. $(Mn,Co)_3O_4$ spinel coatings on ferritic stainless steels for SOFC interconnect applications. Int J Hydrogen Energy 2007;32:3648-54. https://doi.org/10.1016/j.ijhydene.2006.08.048.

[54] Stevenson JW, Yang ZG, Xia GG, Nie Z, Templeton JD. Long-term oxidation behavior of spinel-coated ferritic stainless steel for solid oxide fuel cell interconnect applications. J Power Sources 2013;231:256-63. https://doi.org/10.1016/j.jpowsour.2013.01.033.

[55] Thaheem I, Joh DW, Noh T, Lee KT. Highly conductive and stable $Mn_{1.35}Co_{1.35}Cu_{0.2}Y_{0.1}O_4$ spinel protective coating on commercial ferritic stainless steels for intermediate-temperature solid oxide fuel cell interconnect applications. Int J Hydrogen Energy 2019;44:4293-303. https://doi.org/10.1016/j.ijhydene.2018.12.173.

[56] Saeidpour F, Zandrahimi M, Ebrahimifar H. Evaluation of pulse electroplated cobalt/yttrium oxide composite coating on the Crofer 22 APU stainless steel interconnect. Int J Hydrogen Energy 2019;44:3157-69. https://doi.org/10.1016/j.ijhydene.2018.12.062.

[57] Yang Z, Xia GG, Maupin GD, Stevenson JW. Conductive protection layers on oxidation resistant alloys for SOFC interconnect applications. Surf Coatings Technol 2006;201:4476-83. https://doi.org/10.1016/j.surfcoat.2006.08.082.

[58] Fang Y, Wu C, Duan X, Wang S, Chen Y. High-temperature oxidation process analysis

of $MnCo_2O_4$ coating on Fe-21Cr alloy. Int J Hydrogen Energy 2011;36:5611-6. https://doi.org/10.1016/j.ijhydene.2011.01.130.

[59] Pikalova EY, Kalinina EG. Electrophoretic deposition in the solid oxide fuel cell technology: Fundamentals and recent advances. Renew Sustain Energy Rev 2019;116:109440. https://doi.org/10.1016/j.rser.2019.109440.

[60] Hu S, Li W, Finklea H, Liu X. A review of electrophoretic deposition of metal oxides and its application in solid oxide fuel cells. Adv Colloid Interface Sci 2020;276:102102. https://doi.org/10.1016/j.cis.2020.102102.

[61] Aznam I, Mah JCW, Muchtar A, Somalu MR, Ghazali MJ. Electrophoretic deposition of $(Cu,Mn,Co)_3O_4$ spinel coating on SUS430 ferritic stainless steel: Process and performance evaluation for solid oxide fuel cell interconnect applications. J Eur Ceram Soc 2021;41:1360-73. https://doi.org/10.1016/j.jeurceramsoc.2020.09.074.

[62] Talic B, Falk-Windisch H, Venkatachalam V, Hendriksen PV, Wiik K, Lein HL. Effect of coating density on oxidation resistance and Cr vaporization from solid oxide fuel cell interconnects. J Power Sources 2017;354:57-67. https://doi.org/10.1016/j.jpowsour.2017.04.023.

[63] Talic B, Molin S, Wiik K, Hendriksen PV, Lein HL. Comparison of iron and copper doped manganese cobalt spinel oxides as protective coatings for solid oxide fuel cell interconnects. J Power Sources 2017;372:145-56. https://doi.org/10.1016/j.jpowsour.2017.10.060.

[64] Molin S, Jasinski P, Mikkelsen L, Zhang W, Chen M, Hendriksen P V. Low temperature processed $MnCo_2O_4$ and $MnCo_{1.8}Fe_{0.2}O_4$ as effective protective coatings for solid oxide fuel cell interconnects at 750 °C. J Power Sources 2016;336:408-18. https://doi.org/10.1016/j.jpowsour.2016.11.011.

[65] Froitzheim J, Canovic S, Nikumaa M, Sachitanand R, Johansson LG, Svensson JE.

Long term study of Cr evaporation and high temperature corrosion behaviour of Co coated ferritic steel for solid oxide fuel cell interconnects. J Power Sources 2012;220:217-27. https://doi.org/10.1016/j.jpowsour.2012.06.092.

[66] Gavrilov N V., Ivanov V V., Kamenetskikh AS, Nikonov A V. Investigations of Mn-Co-O and Mn-Co-Y-O coatings deposited by the magnetron sputtering on ferritic stainless steels. Surf Coatings Technol 2011;206:1252-8. https://doi.org/10.1016/j.surfcoat.2011.08.036.

[67] Abdoli H, Molin S, Farnoush H. Effect of interconnect coating procedure on solid oxide fuel cell performance. Mater Lett 2020;259:126898. https://doi.org/10.1016/j.matlet.2019.126898.

[68] Zanchi E, Ignaczak J, Kamecki B, Jasiński P, Molin S, Boccaccini AR, et al. Manganese cobalt-based spinel coatings processed by electro- phoretic deposition method : the influence of sintering on deg- radation issues of Solid Oxide Cell oxygen electrodes at 750°C. Materials (Basel) 2021;14:3836. https://doi.org/https://doi.org/10.3390/ma14143836.

[69] VDM ® Crofer 22 APU. Material Datasheet no. 4046, vol. 10; 2010. n.d. https://www.vdm-metals.com/fileadmin/user_upload/Downloads/Data_Sheets/Data_Sheet_VDM_Crofer_22_APU.pdf (accessed July 13, 2021).

[70] Pan Y, Geng S, Chen G, Wang F. Effect of pre-oxidation on surface scale microstructure and electrical property of Cu-Fe coated steel interconnect. Corros Sci 2020;170:108680. https://doi.org/10.1016/j.corsci.2020.108680.

[71] FEI company website - http://www.fei.com; FEI Application note AN0027 07-2010: ChemiSTEM™ Technology, A revolution in EDX analytics. n.d. https://www.fei.com/#gsc.tab=0 (accessed July 13, 2021).

[72] Mrowec S. An Introduction to the Theory of Metal Oxidation. Washington, D.C.: National Bureau of Standards and National Science Foundation,; 1982.

[73] Kofstad P. High-Temperature Oxidation of Metals. New York-London-Sydney: Inc., John Wiley & Sons; 1978.

[74] Molin S. Evaluation of electrodeposited Mn-Co protective coatings on Crofer 22 APU steel. Int J Appl Ceram Technol 2018;15:349-60. https://doi.org/10.1111/ijac.12816.

[75] Chen L, Sun EY, Yamanis J, Magdefrau N. Oxidation Kinetics of $Mn_{1.5}Co_{1.5}O_4$-Coated Haynes 230 and Crofer 22 APU for Solid Oxide Fuel Cell Interconnects. J Electrochem Soc 2010;157:B931. https://doi.org/10.1149/1.3391820.

[76] Qu W, Jian L, Hill JM, Ivey DG. Electrical and microstructural characterization of spinel phases as potential coatings for SOFC metallic interconnects. J Power Sources 2006;153:114-24. https://doi.org/10.1016/j.jpowsour.2005.03.137.

[77] Seo HS, Jin G, Jun JH, Kim DH, Kim KY. Effect of reactive elements on oxidation behaviour of Fe-22Cr-0.5Mn ferritic stainless steel for a solid oxide fuel cell interconnect. J Power Sources 2008;178:1-8. https://doi.org/10.1016/j.jpowsour.2007.12.026.

[78] Jedlinski J, Borchardt G, Konopka M, Nocun M. The effect of reactive elements on the oxidation behaviour of Fe23Cr5Al alloys at high temperatures I. Kinetics and thermal cycling. Solid State Ionics 1997;101-103:1147-55. https://doi.org/10.1016/s0167-2738(97)00302-0.

[79] Pint BA. Experimental observations in support of the dynamic-segregation theory to explain the reactive-element effect. Oxid Met 1996;45:1-37. https://doi.org/10.1007/BF01046818.

[80] Wright IG, Wilcox BA. The oxidation of Fe-Cr alloys containing an oxide dispersion or reactive metal additions. Oxid Met 1974;8:283-301.

https://doi.org/10.1007/BF00609945.

[81] Pint BA, Garratt-Reed AJ, Hobbs LW. The reactive element effect in commercial ODS fecrai alloys. Mater High Temp 1995;13:3-16. https://doi.org/10.1080/09603409.1995.11689496.

[82] Ferrari AC, Roberston J. Interpretation of Raman spectra of disordered and amorphous carbon. Phys Rev B - Condens Matter Mater Phys 2000;61:14095. https://doi.org/10.1007/BF02543692.

[83] Kovanda F, Rojka T, Dobešová J, MacHovič V, Bezdička P, Obalová L, et al. Mixed oxides obtained from Co and Mn containing layered double hydroxides: Preparation, characterization, and catalytic properties. J Solid State Chem 2006;179:812-23. https://doi.org/10.1016/j.jssc.2005.12.004.

[84] Meena PL, Pal S, Sreenivas K, Kumar RA. Structural and magnetic properties of $MnCo_2O_4$ spinel multiferroic. Adv Sci Lett 2015;21:2760-3. https://doi.org/10.1166/asl.2015.6336.

[85] Yuvaraj S, Vignesh A, Shanmugam S, Kalai Selvan R. Nitrogen-doped Multi-walled Carbon Nanotubes-$MnCo_2O_4$ microsphere as electrocatalyst for efficient oxygen reduction reaction. Int J Hydrogen Energy 2016;41:15199-207. https://doi.org/10.1016/j.ijhydene.2016.06.115.

[86] Stelmachowski P, Monteverde Videla AHA, Ciura K, Specchia S. Oxygen evolution catalysis in alkaline conditions over hard templated nickel-cobalt based spinel oxides. Int J Hydrogen Energy 2017;42:27910-8. https://doi.org/10.1016/j.ijhydene.2017.06.034.

[87] Hosterman BD. Raman Spectroscopic Study of Solid Solution Spinel Oxides. University of Nevada, 2011.

[88] Romaguera-Barcelay Y, Agostinho Moreira J, Almeida A, Tavares PB, Pérez De La

Cruz J. Structural, electrical and magnetic properties of magnetoelectric $GdMnO_3$ thin films prepared by a sol-gel method. Thin Solid Films 2014;564:419-25. https://doi.org/10.1016/j.tsf.2014.06.007.

[89] Tiwari P, Kumar S, Rath C. Probing structural transformation and optical and magnetic properties in Cr doped $GdMnO_3$: Jahn-Teller distortion, photoluminescence and magnetic switching effect. RSC Adv 2019;9:39871-82. https://doi.org/10.1039/c9ra08562a.

[90] Mahana S, Pandey SK, Rakshit B, Nandi P, Basu R, Dhara S, et al. Site substitution in GdMnO3: Effects on structural, electronic, and magnetic properties. Phys Rev B 2020;102. https://doi.org/10.1103/PhysRevB.102.245120.

[91] Le Luyer C, García-Murillo A, Bernstein E, Mugnier J. Waveguide Raman spectroscopy of sol-gel Gd_2O_3 thin films. J Raman Spectrosc 2003;34:234-9. https://doi.org/10.1002/jrs.980.

[92] Julien CM, Massot M, Poinsignon C. Lattice vibrations of manganese oxides: Part I. Periodic structures. Spectrochim Acta - Part A Mol Biomol Spectrosc 2004;60:689-700. https://doi.org/10.1016/S1386-1425(03)00279-8.

[93] Bernardini S, Bellatreccia F, Casanova Municchia A, Della Ventura G, Sodo A. Raman spectra of natural manganese oxides. J Raman Spectrosc 2019;50:873-88. https://doi.org/10.1002/jrs.5583.

[94] Kendall K, Kendall M. High-Temperature Solid Oxide Fuel Cells for the 21st Century: Fundamentals, Design and Applications: Second Edition. Elsevier Ltd; 2015. https://doi.org/10.1016/C2011-0-09278-5.

[95] Mougin J, Le Bihan T, Lucazeau G. High-pressure study of Cr_2O_3 obtained by high-temperature oxidation by X-ray diffraction and Raman spectroscopy. J Phys Chem Solids 2001;62:553-63. https://doi.org/10.1016/S0022-3697(00)00215-8.

[96] Zhu WZ, Deevi SC. Development of interconnect materials for solid oxide fuel cells. Mater Sci Eng A 2003;348:227-43. https://doi.org/10.1016/S0921-5093(02)00736-0.

[97] Mazur Ł, Molin S, Dąbek J, Durczak K, Pyzalski M, Brylewski T. Physicochemical properties of $Mn_{1.45}Co_{1.45}Cu_{0.1}O_4$ spinel coating deposited on the Crofer 22 H ferritic steel and exposed to high-temperature oxidation under thermal cycling conditions. J Therm Anal Calorim 2021. https://doi.org/10.1007/s10973-021-10884-2.

[98] Jiang SP, Zhang S, Zhen YD. Deposition of Cr Species at $(La,Sr)(Co,Fe)O_3$ Cathodes of Solid Oxide Fuel Cells. J Electrochem Soc 2006;153:A127. https://doi.org/10.1149/1.2136077.

List of figure captions

Fig. 1. Oxidation kinetics plots for investigated samples oxidized over 7000 h in air at 1073 K: A) linear plot, B) parabolic plot.

Fig. 2. SEM micrographs of polished sample cross-sections and the X-ray diffraction patterns recorded for the studied samples after 7000 h of oxidation in air at 1073 K: A) Crofer 22 APU, B) Crofer 22 APU/MC, C) Crofer 22 APU/Gd, D) Crofer 22 APU/Gd/MC, E) X-ray diffraction patterns.

Fig. 3. Triple junction in Cr_2O_3 grains – S/TEM-HAADF image (A) and respective areas marked with squares under increasing magnification (B, C).

Fig. 4. S/TEM-HAADF image of the grain boundary (A), element distribution maps of Gd and Cr determined via S/TEM-EDS(B,C), and EDS line scan analysis for Gd, Cr and O across the white dotted line in Fig. 5A (D).

Fig. 5. Confocal Raman imaging of the cross-section of the Crofer 22 APU/Gd/MC sample oxidized at 1073 K for 7000 h: A) confocal image (red square corresponds to area investigated with Raman laser), B) *k*-means cluster analysis, C) combined distribution image, D) overlay bitmap for images A and B. Raman distribution images (obtained via the integration of the most characteristic band for a particular phase along with the value of its Raman shift given in brackets) are complemented with the average Raman spectra: E) resin (1597 cm^{-1}), F) $MnCo_2O_4$ (600 cm^{-1}), G) $GdCr_{1-x}Mn_xO_3$ (620 cm^{-1}), H) Cr_2O_3 (555 cm^{-1}), I) $(Mn,Cr)_3O_4$ (681 cm^{-1}) / MnO_2

(538 cm^{-1}). Each average spectrum is also marked with bands that can be unequivocally attributed to the corresponding phase(s).

Fig. 6. Temperature dependence of area-specific resistance for tested layered systems after 7000 h of oxidation in air at 1073 K, presented in an Arrhenius plots.

Fig. 7. Plots recorded for the examined cells at 1073 K: A) I-V curves, B) Nyquist plot (IC – interconnect).

Fig. 8. Post-mortem SEM images taken for: A) aged fuel cell with Crofer 22 APU/Gd/MC interconnect, B) aged fuel cell with Crofer 22 APU interconnect, C) aged fuel cell without an interconnect, D) EDX spectra for the studied samples.

List of table captions